

# A Frequency Diversity Algorithm for Extending the Radar Doppler Velocity Nyquist Interval

V. Venkatesh\*, L. Li<sup>†</sup>, M. McLinden<sup>†</sup>, M. Coon<sup>†</sup>, G. M. Heymsfield<sup>†</sup>, S. Tanelli\*,  
H. Hovhannisyan\*<sup>‡</sup>

\* Jet Propulsion Laboratory, California Institute of Technology, Pasadena, CA.

<sup>†</sup> NASA/Goddard Space Flight Center, Greenbelt, MD.

<sup>‡</sup> University of California at San Diego, CA.

## Abstract

Compact millimeter wavelength radars have been widely used for applications such as remote sensing of clouds, guidance avionics and recently, automotive navigation. However, the short wavelength of these radars limits their maximum unambiguous Doppler velocity. A common solution to this problem is to subsequently unfold the Doppler velocity estimate with the staggered pulse repetition time (PRT) algorithm, which requires two different PRTs to be employed in sequence. This work investigates a potentially more rapid method to extend the Doppler velocity Nyquist interval. We estimate Doppler velocity using a pair of frequency diverse pulses separated by a time lag that is significantly shorter than the PRT. During the first PRT, two pulses with center frequencies  $f_1$  followed by  $f_2$  separated by a lag  $\tau$  are transmitted. During the next PRT, the pulses transmitted are in the order  $f_2$  followed by  $f_1$ . Doppler velocity is then estimated using the sum of the Doppler phases derived from  $f_1/f_2$  and  $f_2/f_1$  sequences. Similar frequency diverse Doppler estimation algorithms have been investigated for automotive radars. The focus of this work is the demonstration in a beam-filled scenario and the error canceling algorithm design. Based on Monte-Carlo simulations and data collected with the NASA Goddard Space Flight center (GSFC) Cloud Radar System (CRS), the algorithm is demonstrated on nearly static surface echoes. Projected aircraft speeds and traditional pulse-pair estimates are employed

25 as references. The algorithm was found to perform adequately on surface echoes for a low spectrum  
 26 width of the order of 0.5 m/s and SNR comparable to 20 dB. A simple point-target based model is  
 27 used to interpret results, and simulations are used as a baseline to transition from point-target to surface  
 28 scattering scenarios. Doppler velocity retrievals in a cirrus cloud with low velocity turbulence retained  
 29 some qualitative structure, albeit with significantly degraded precision due to the lost coherence.

30 **Index Terms**

31 Millimeter wave radar, algorithm design, data analysis, signal processing, Doppler velocity. Fre-  
 32 quency diversity, pulse-pair.

33 **I. INTRODUCTION**

34 Millimeter wave radars have been used for applications such as atmospheric remote sensing  
 35 [1], [2], [3], target tracking [4], [5], guidance and navigation [6], [7]. In part, the popularity of  
 36 these millimeter wave radars is because short wavelengths ( $\lambda$ ) allow fine angular resolution to  
 37 be realized while still allowing for physically small and lightweight designs. The choice of a  
 38 short wavelength however exacerbates the range-Doppler ambiguity dilemma in pulse trains. For  
 39 a given pulse repetition time ( $T$ ), the unambiguous Doppler velocity ( $v_u$ ) is given by  $v_u = \frac{\lambda}{4T}$   
 40 while the unambiguous range ( $R_u$ ) is given by  $R_u = \frac{cT}{2}$ . Given that pulse repetition time is  
 41 directly proportional to  $R_u$  but inversely proportional to  $v_u$ , the resultant trade is exacerbated  
 42 at short wavelengths. As a consequence, long range millimeter wavelength radars often have  
 43 Doppler Nyquist intervals that are much smaller than the relative target speeds with respect to  
 44 the platform.

45 Techniques to mitigate this Doppler-Range ambiguity dilemma have been developed. For  
 46 example, the staggered PRT [8] and Polarization Diversity Pulse-Pair (PDPP) [9] techniques  
 47 decouple the maximum unambiguous range from the maximum unambiguous Doppler velocity.  
 48 The staggered PRT is a multi-rate sampling method that unfolds the Doppler velocity based  
 49 on differential aliasing in Doppler velocities measured using 2 unique Pulse Repetition Times  
 50 (PRT). The idea is that as the true velocity increases, it aliases onto different values within  
 51 the two Doppler Nyquist intervals. Depending on the difference in measured Doppler velocities  
 52 from the 2 PRTs, a correction is computed. A limitation of the staggered PRT method is that  
 53 the dwell time approaches double that of single PRT operation. This is because of the need to

54 estimate Doppler velocity with sufficient precision sequentially at two lags. In the Polarization  
55 Diversity Pulse-Pair (PDPP) method, two pulses with orthogonal polarizations are placed within  
56 a PRT and Doppler velocity is estimated by cross-correlating voltages from these two pulses  
57 with orthogonal polarizations. The unambiguous Doppler velocity now corresponds to the lag  
58 between the pair of pulses with orthogonal polarizations, while the unambiguous range still  
59 corresponds to the PRT. For non-depolarizing scatterers, the cross-polarization isolation of the  
60 antenna provides a mechanism to isolate returns from each polarization. A limitation of this  
61 method is the need for additional microwave hardware such as an orthomode transducer and  
62 dual-polarized feeds for the antenna. But the inevitable spillage due to finite cross-polarization  
63 isolation hinders the applicability of this approach in low SNR regions of the range profile that  
64 are contiguous to high SNR regions. For nadir looking radars, the ever present surface echo  
65 makes the PDPP retrieval of Doppler velocity difficult in low altitude regions [10].

66 This work investigates a novel application of an algorithm that uses frequency diverse wave-  
67 forms for Doppler velocity estimation [11] [12]. Relative to the analogous polarization diversity  
68 pulse-pair algorithm, isolation is traded for coherence. For applications where this loss in coher-  
69 ence is not precipitous, digital filters provide isolation that is several orders of magnitude better  
70 than antenna cross-polarization isolation at millimeter wavelengths. Similar methods have been  
71 formulated for use in automotive radars [13], and the novel part herein is the error canceling  
72 algorithm design and subsequent demonstration to a beam-filled scenario with non-zero spectrum  
73 width. The methods used involve numerical simulations and analysis of surface echo data.  
74 The following section outlines a conceptual formulation of the Frequency Diversity Pulse-Pair  
75 algorithm (FDPP) using a point-target model. Numerical simulations are then employed as a  
76 baseline to transition from point-target to surface scattering scenarios. Finally, surface echo data  
77 is used to demonstrate the algorithm using projected aircraft speeds and traditional pulse-pair  
78 measurements as references.

## 79 II. ALGORITHM FORMULATION

80 The algorithm investigated herein decouples unambiguous velocity from unambiguous range  
81 by employing two frequency shifted waveforms within a pulse repetition period. As shown in  
82 Fig. 1, the two transmitted pulses at center frequencies of  $f_1$  and  $f_2$  are separated by a time-  
83 lag  $\tau$ . The order of transmitted frequencies is reversed after every transmit/receive cycle while

84 retaining the same lag  $\tau$ . The choice of  $f_1$  and  $f_2$  is such that the return signals can be separated  
 85 by filters implemented in the digital receiver. Cross-covariances from the two sequences are  
 86 individually accumulated and stored (denote as  $c_{12}$  and  $c_{21}$  respectively). Doppler velocity is  
 87 then estimated from the sum of the cross-covariance estimates from each pair.

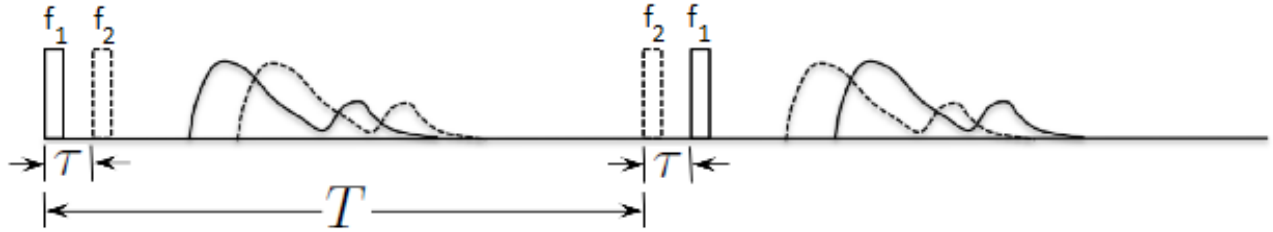


Fig. 1: Illustration of the Frequency Diversity Pulse-Pair (FDPP) algorithm concept. The first sequence transmitted has two frequencies  $f_1$  followed by  $f_2$  and separated by lag  $\tau$ . After one elapsed pulse-repetition time  $T$ , the next transmitted sequence has  $f_2$  followed by  $f_1$  separated by the same lag  $\tau$ . The concept is that errors and range dependent phase terms between the  $f_1/f_2$  and  $f_2/f_1$  pairs cancel out.

88 Herein, a simple point target based analysis of the phase estimate produced by the FDPP  
 89 algorithm is presented. Denote the received voltage at the antenna at frequency  $f_1$  due to a  
 90 point-target at range  $R$  as [14] and slow-time  $t = 0$  as

$$V_1(R, 0) = S_1 \exp\{-2jk_1 R\}. \quad (1)$$

91 For the same range-bin of interest, the received voltage at frequency 2 after a time-lag  $\tau$ , can  
 92 be written as

$$V_2(R, \tau) = S_2 \exp\{-2jk_2(R + v_r \tau)\}, \quad (2)$$

93 where  $v_r$  is the radial velocity of the scatterer towards or away from the radar,  $S_1$  and  $S_2$   
 94 are radar system dependent constants. Since the radial component of velocity causes the most  
 95 phase shifts, it suffices to consider this component of scatterer motion alone. Note that we have  
 96 neglected the backscattered phase contribution to the received signal at the two frequencies. Based  
 97 on [15], it can be shown that as long as the difference in backscattered phase between the two  
 98 frequencies is small, their effect on Doppler velocity estimates is negligible. The instantaneous  
 99 complex conjugated voltage product from the  $f_1/f_2$  pair is

$$c_{12}(R, \tau) = V_1^* V_2 \approx S_1 S_2 \exp\{-[2j(k_2 - k_1)R + (2k_2 v_r \tau)]\}. \quad (3)$$

100 During the next pulse repetition interval, this becomes

$$c_{21}(R, \tau) = V_2^* V_1 \approx S_1 S_2 \exp\{-[2j(k_1 - k_2)R + (2k_1 v_r \tau)]\}. \quad (4)$$

101 To proceed, we assume the random process to be wide-sense stationary and completely  
 102 described by the lag  $\tau$ . The dependence on starting time is therefore omitted. Consider the  
 103 estimator

$$\langle c(R, \tau) \rangle = \frac{1}{M} \sum_{i=1}^M [c_{12}(R, \tau) + c_{21}(R, \tau)]. \quad (5)$$

104 where the number of pulses  $M$  is sufficiently large such that the ensemble average approximates  
 105 the expected value. Denote the phase of  $c(R, \tau)$  as  $\Delta\Phi$ , the phases of  $c_{12}(R, \tau)$  and  $c_{21}(R, \tau)$   
 106 as  $\Delta\phi_{12}$  and  $\Delta\phi_{21}$  respectively. Assuming that the magnitude expectations of  $c_{12}(R, \tau)$  and  
 107  $c_{21}(R, \tau)$  are equal, we get

$$\langle \Delta\Phi \rangle = \langle \Delta\phi_{12} + \Delta\phi_{21} \rangle. \quad (6)$$

108 In arriving at the above relationship, we have factored the expectations of  $c_{12}(\tau)$  and  $c_{21}(\tau)$   
 109 by recognizing addition to be a linear operator. Using (3) and (4) in (6), we can relate the phase  
 110  $\Delta\Phi$  to radial velocity as

$$\langle \Delta\Phi \rangle = 2(k_1 + k_2)\tau v_r. \quad (7)$$

111 The implementation we consider herein typically has frequencies that are separated by several  
 112 MHz for a millimeter wave radar, such as a 94 GHz W-band radar system. In this specific case,  
 113 we approximate  $k_1 + k_2 \approx 2k_1$ . The above equation now simplifies to

$$v_r = \frac{1}{4k_1\tau} \langle \Delta\Phi \rangle. \quad (8)$$

114 Since all values other than  $\Delta\Phi$  are solely system dependent, the radial component of target  
 115 mean radial velocity  $v_r$  can be obtained from the ensemble-averaged  $\Delta\Phi$ . Two comments about  
 116 the Nyquist velocity of the frequency diversity pulse-pair estimates are in order. First, the  
 117 frequency diversity pulse-pair algorithm developed herein allows an extension of the Nyquist  
 118 interval as compared to a traditional pulse-pair. This is because  $\tau \ll T$ . Second, for a given  
 119 lag  $\tau$  the Nyquist interval is diminished by a factor of 2 compared to a traditional pulse-pair or

120 a polarization diversity pulse-pair. This is because the frequency diversity pulse-pair algorithm  
 121 accumulates two phase estimates  $\Delta\phi_{12}$  and  $\Delta\phi_{21}$  and each of these variables that form the  
 122 resultant sum have a range of variation from  $[-\pi, \pi]$ . In summary, if the FDPP estimate is  
 123 obtained with a lag  $\tau$  and the traditional pulse-pair estimate is obtained with a lag  $T$ , then the  
 124 Nyquist interval of the FDPP algorithm is improved by a factor  $\frac{T}{2\tau}$ .

125 While the expected value of the frequency diverse pulse-pair converges to a phase that is  
 126 linearly proportional to Doppler velocity, the algorithm is only practical if random errors are  
 127 comparable to traditional pulse-pairs. This random error of the frequency diverse pulse-pair  
 128 algorithm significantly benefits from anti-correlation between the  $f_1/f_2$  and  $f_2/f_1$  pulse-pairs.  
 129 A decomposition of the variance of  $\Delta\Phi$  shows that the anti-correlation between the frequency  
 130 diverse pulse-pair phases partially alleviates the loss of pulse-pair coherence due to Rayleigh  
 131 fading. Let  $Var$  denote the variance operator,  $Cov$  denote the covariance operator and  $\rho$  denote  
 132 the correlation operator for the random variables  $\Delta\Phi_{12}$  and  $\Delta\Phi_{21}$ . From (6), we know that

$$Var(\Delta\Phi) = Var(\Delta\Phi_{12}) + Var(\Delta\Phi_{21}) + 2Cov(\Delta\Phi_{12}, \Delta\Phi_{21}) \quad (9)$$

133 Now, the covariance term can be conveniently decomposed as

$$Cov(\Delta\Phi_{12}, \Delta\Phi_{21}) = \rho(\Delta\Phi_{12}, \Delta\Phi_{21}) \cdot \sqrt{Var(\Delta\Phi_{12}) \cdot Var(\Delta\Phi_{21})} \quad (10)$$

134 Since the same time-lag  $\tau$  is used for the  $f_1/f_2$  pair and the  $f_2/f_1$  pair,  $Var(\Delta\Phi_{12}) =$   
 135  $Var(\Delta\Phi_{21})$ ,

$$Cov(\Delta\Phi_{12}, \Delta\Phi_{21}) = \rho(\Delta\Phi_{12}, \Delta\Phi_{21}) \cdot Var(\Delta\Phi_{12}) \quad (11)$$

136 From the above relationships,

$$Var(\Delta\Phi) = 2Var(\Delta\Phi_{12}) + 2\rho(\Delta\Phi_{12}, \Delta\Phi_{21}) \cdot Var(\Delta\Phi_{12}) \quad (12)$$

137 Rearranging terms in (12),

$$Var(\Delta\Phi) = 2Var(\Delta\Phi_{12})[1 + \rho(\Delta\Phi_{12}, \Delta\Phi_{21})] \quad (13)$$

138 From (13), we see that as  $\rho(\Delta\Phi_{12}, \Delta\Phi_{21})$  tends to -1,  $Var(\Delta\Phi)$  tends to 0. In other words,  
 139 the variances of the  $f_1/f_2$  and  $f_2/f_1$  phase estimates can be large since there is little correlation  
 140 between the  $f_1$  and  $f_2$  pulses. However, if the  $f_1/f_2$  and  $f_2/f_1$  phase estimates are highly anti-  
 141 correlated, the sum of the two phase estimates has a much smaller variance. For sufficiently small

<sup>142</sup> Doppler velocities in (3) and (4), it can be shown than  $\rho(\Delta\Phi_{12}, \Delta\Phi_{21}) = -\rho(\Delta\Phi_{12}, \Delta\Phi_{12})$ . For  
<sup>143</sup> low velocity turbulence and short lags, it appears reasonable to approximate the auto-correlation  
<sup>144</sup>  $\rho(\Delta\Phi_{12}) \approx 1$ . This is turn results in  $\rho(\Delta\Phi_{12}, \Delta\Phi_{21}) \approx -1$ .

<sup>145</sup> Note that a similar identity was first exploited on contiguous pulse-pairs [16]. The difference  
<sup>146</sup> here is that alternating  $f_1/f_2$  and  $f_2/f_1$  pairs brings about an anti-correlation, as opposed to  
<sup>147</sup> the “common pulse” in contiguous pulse-pairs. The algorithm herein has more similarities  
<sup>148</sup> to the alternating polarization sequence used for “Differential propagation phase shift” ( $\Phi_{DP}$ )  
<sup>149</sup> measurements in [15]. In that case, it was shown that the correlation between phase estimates  
<sup>150</sup> from an alternately reversing sequence approaches -1 for zero spectrum width and  $SNR > 20$   
<sup>151</sup> dB (equation 6.57 in [17]).

### <sup>152</sup> III. PERFORMANCE EVALUATION

#### <sup>153</sup> A. Simulations

<sup>154</sup> The point-target based model in the earlier section was solely meant to aid interpretation.  
<sup>155</sup> Numerical simulations are used as a baseline to go from point-target to beam-filled scattering.  
<sup>156</sup> The approach to simulations adopted herein is to compute backscattered voltages using a Monte-  
<sup>157</sup> Carlo like simulator [18] and estimate the phases at lag  $\tau$  on the simulated voltages. The voltage  
<sup>158</sup> at the radar receiver due to a collection of scatterers is given as

$$V(t) = \beta \sum_{n=1}^{N_s} A_n R_n \exp\{-2jkr_n\}. \quad (14)$$

<sup>159</sup> Here,  $\beta$  is the radar constant for beam-filled surface scattering. Further,  $n$  denotes the  $n^{th}$   
<sup>160</sup> scatterer,  $A_n$  denotes the antenna weighting function and  $R_n$  denotes the range weighting function  
<sup>161</sup> evaluated for the  $n^{th}$  scatterer. The antenna weighting function is defined below

$$A(X_n, Y_n) = \exp \left\{ -\frac{(X_0 - X_n)^2}{2r_0^2 \sigma_\phi^2} - \frac{(Y_0 - Y_n)^2}{2r_0^2 \sigma_\theta^2} \right\} \quad (15)$$

<sup>162</sup> where the antenna phase center is denoted by  $[X_0, Y_0]$  and is the origin for the co-ordinate  
<sup>163</sup> system adopted herein. The scatterer locations are indicated by  $[X_n, Y_n]$  and  $\sigma_\phi$  and  $\sigma_\theta$  are the  
<sup>164</sup> second central moments of the effective two way antenna patterns in the azimuthal and elevation  
<sup>165</sup> planes respectively. These are related to antenna 3-dB beamwidths by the relationship

$$\sigma_\phi = \frac{\theta_{3dB}}{\sqrt{(8 * \ln 2)}} \quad (16)$$

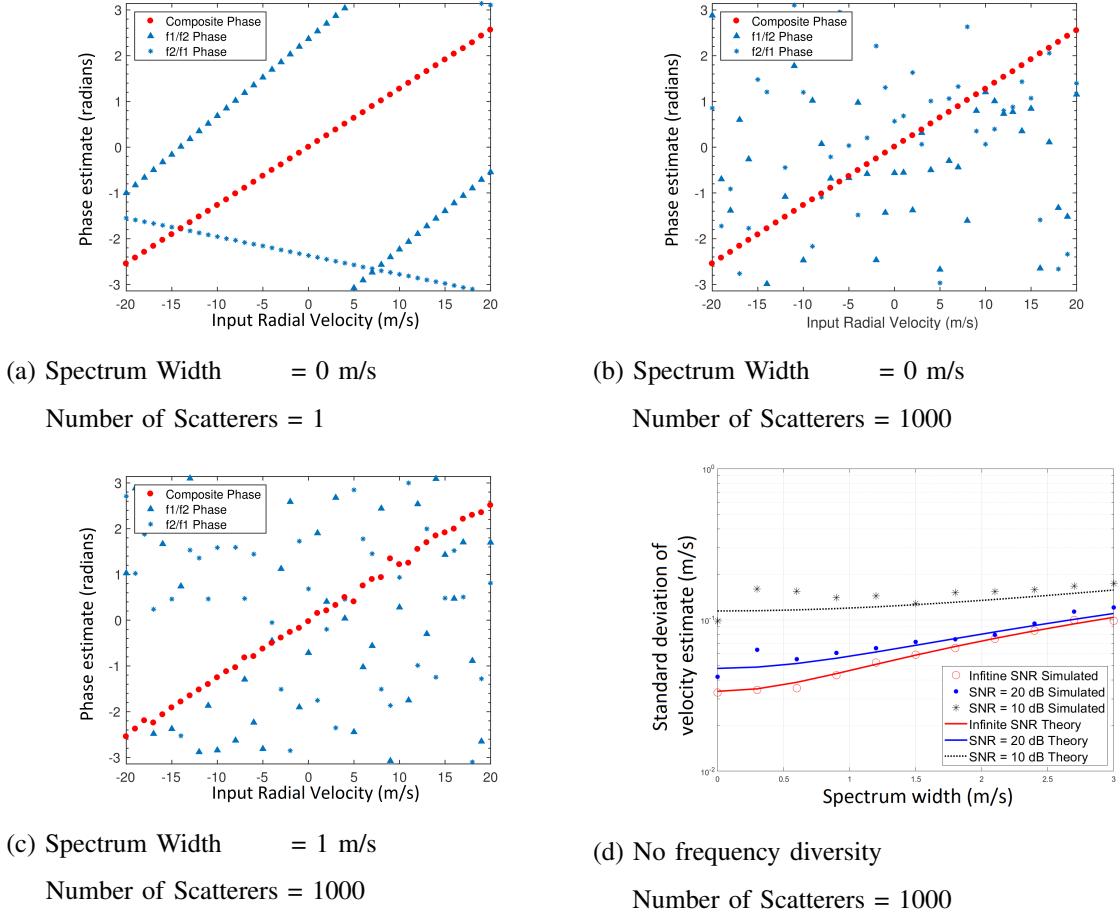


Fig. 2: Monte-Carlo simulations showing the frequency diversity Doppler estimation algorithm concept. Figures (a)-(c) have a frequency diversity of 5 MHz. As the number of scatterers increase, the  $f_1/f_2$  and  $f_2/f_1$  pair phases become increasingly “noisy”. But the composite phase (sum of  $f_1/f_2$  and  $f_2/f_1$  phases) has a linear dependence on Doppler velocity for small spectrum width. Simulation parameters : Radar frequency  $f = 95$  GHz, PRT = 200  $\mu$ s, antenna 3-dB beamwidth  $\theta_{3dB} = 3$  deg, Range  $R = 10$  km, dwell time  $T_d = 100$  ms, x- and y-component of scatterer advection  $v_x = 0$  m/s and  $v_y = 0$  m/s. Figure (d) compares simulated statistics of radial velocity estimates with theoretical expectations for no frequency diversity in [17].

where,  $\theta_{3dB}$  denotes the antenna 3 dB beamwidth. The range weighting function is given by

$$R(Z_n) = \exp \left\{ -\frac{(Z_0 - Z_n)^2}{2\sigma_R^2} \right\} \quad (17)$$

where,  $Z_0$  is the range to the center of the resolution volume and  $Z_n$  indicates the scatterer

location [18]. The location of each scatterer is updated at every pulse repetition interval  $\tau$  using the relationship  $\vec{P}_n = \vec{P}_n + \vec{v}_n\tau$ . Here,  $\vec{P}_n$  denotes the three-dimensional position of the scatterer and  $\vec{v}_n$  denotes the velocity of each scatterer. Each component of three-dimensional velocity is in turn decomposed into deterministic and random velocity components. Gaussian distributed zero-mean random variables are used to synthesize the turbulent velocity fields. As the scatterers evolve, the voltages at the frequencies of interest are obtained in a manner consistent with Fig. 1. After scaling to the desired SNR, thermal noise is added to the synthesized signals at the respective frequencies before the phase estimates are produced, after scaling for the desired SNR. Phase estimates at the lag  $\tau$  are then obtained for the sequences  $f_1/f_2$  and  $f_2/f_1$ , added and subsequently scaled using equation (8) to obtain Doppler velocity.

Fig. 2 shows simulated estimates of Doppler velocity using the frequency diverse algorithm for a dwell time of 100 ms. Here, “composite phase” is the sum of the  $f_1/f_2$  and  $f_2/f_1$  phases after wrapping into the interval  $[-\pi, \pi]$ . As is evident in Fig. 2a, the algorithm works well for a point scatterer. As the number of scatterers alone is increased, the estimator still holds up well. But the combination of Rayleigh fading and spectrum width degrades the precision of the Doppler estimate (see Fig. 2c). This algorithm is therefore limited to beam-filled scenarios with low spectrum width. Finally, the simulated statistics of radial velocity are in reasonable agreement with theoretical expectations for no frequency diversity [17]. The following section uses numerical simulations package validated in Fig. 2d as a baseline to interpret data analysis results.

### 188 B. Data analysis

To evaluate performance, the FDPP technique was implemented on the NASA Goddard Space Flight Center (GSFC) W-band Cloud Radar System (CRS) during the 2015 NASA Olympic Mountain Experiment (OLYMPEX) and the 2017 NOAA Geostationary Operational Environmental Satellite R (GOES-R) series calibration campaign. During these field campaigns, CRS was installed on the NASA ER-2 aircraft along with the other sensors for cloud and precipitation observation. The antenna was pointed near nadir. Fig. 3 shows qualitative comparisons of FDPP retrievals on isolated surface echoes with traditional pulse-pair measurements. Simulations are used as a baseline to interpret differences between traditional pulse-pair and FDPP Doppler estimates. Pointing angle deviations away from nadir are introduced because of antenna mounting

198 errors and aircraft attitude. In turn, this induces a non-zero surface velocity measurement due the  
 199 motion of the aircraft. In Fig. 3, “Measured pulse-pair velocities” shown in Fig. 3a and the error  
 200 sources shown in Fig. 3b were used as inputs to the simulation. The simulation output is shown  
 201 by the red dotted line in Fig. 3a and aids interpretation of the FDPP algorithm performance.

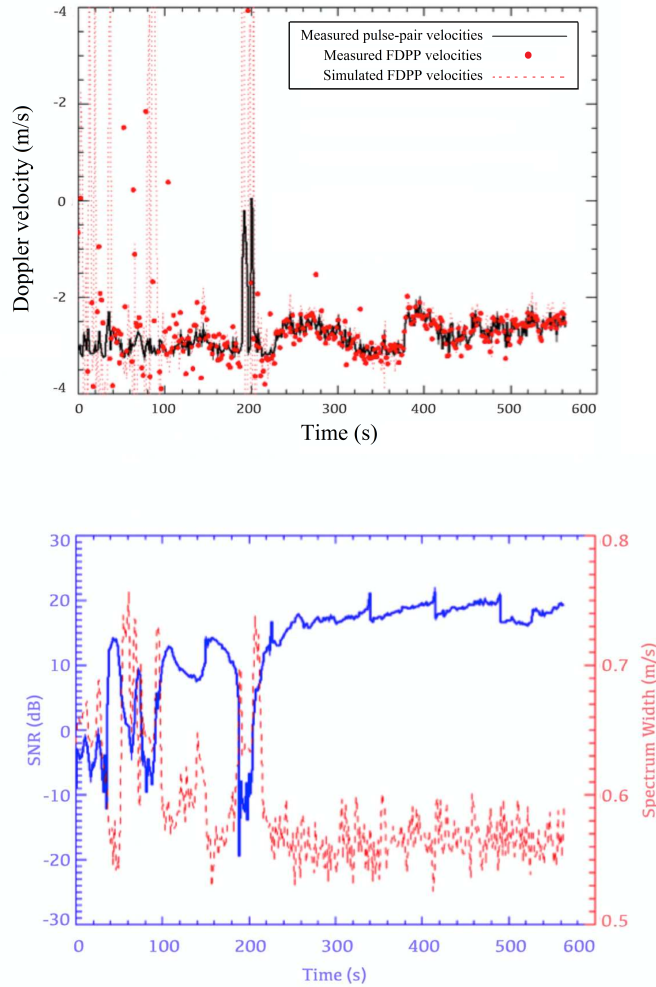


Fig. 3: Top - Evaluation of frequency diversity Doppler velocity measurements using traditional pulse-pair measurements as a reference. Simulations are employed as a baseline for interpretation. While the FDPP algorithm performs well for SNR of the order of 20 dB, both measurements and simulations show that the algorithm has poor immunity to thermal noise. Bottom - SNR and spectrum width corresponding to the duration over which the measurements were made. The “blue” line corresponds to SNR in dB and the “red” line corresponds to Spectrum width in m/s.

202 First, FDPP estimates of Doppler velocity are in reasonable agreement with traditional pulse-  
 203 pair Doppler velocity estimates in regions of high SNR (i.e. of the order of 20 dB). Second, both  
 204 FDPP measurements from CRS and simulations show large deviations from traditional pulse-pair  
 205 Doppler velocity estimates in regions of low SNR (i.e. comparable to 0 dB). This is because the  
 206 error cancellation mechanism of the FDPP algorithm relies on high anti-correlation between the  
 207  $f_1/f_2$  pair and the  $f_2/f_1$  pair, whereas thermal noise has zero correlation at time-lag  $\tau$ .

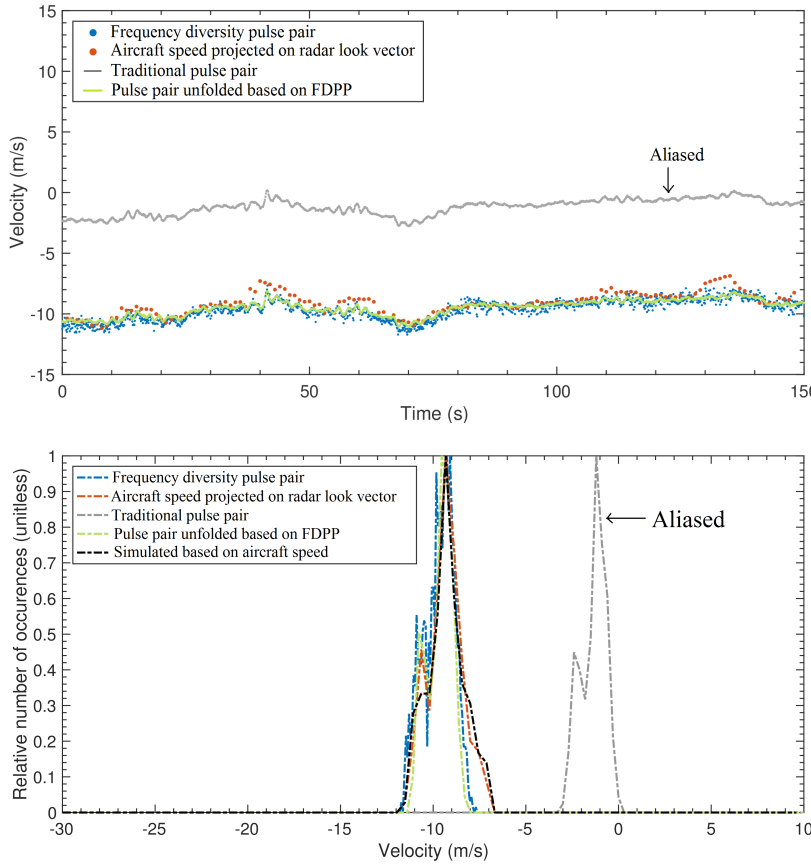


Fig. 4: Comparison of FDPP and traditional pulse-pair measurements of surface echo Doppler velocity using projected aircraft speed as a reference. Top - While traditional pulse-pair estimates are aliased, FDPP estimates of Doppler velocity agree with aircraft speed projections on the radar look vector. However, unfolded pulse-pair velocities using the pulse-pair as reference show that the FDPP has a higher standard deviation relative to the traditional pulse-pair estimator. Bottom - The probability density functions of simulated FDPP Doppler estimates are in qualitative agreement with measurements. The simulations herein used projected aircraft speeds as input.

208 During one of the GOES-R flights, the ER-2 aircraft pilot performed pitch maneuvers. For one  
209 of these measurements with significant pitch, Fig. 4 shows FDPP measurements of surface echo  
210 Doppler velocity compared to conventional pulse-pair velocities using projected aircraft speed  
211 as a reference. The aircraft attitude was recorded using an Inertial Motion Unit and measured  
212 velocity, roll, pitch, and heading. The geometric projection of the aircraft motion vector onto the  
213 radar look vector gives the radial velocity that is employed as a reference herein. To compute this  
214 projection, two coordinate systems are defined; aircraft relative and track relative. The aircraft  
215 relative coordinate system expresses the orientation of the aircraft for a given attitude. However,  
216 the track relative coordinate system is assumed to be static. The rotation of the aircraft relative  
217 coordinate system was mapped to track relative coordinate system using the rotation matrices  
218 defined in [19].

219 Using the projected radial velocity as a reference, we note that the FDPP measurements  
220 of Doppler velocity are in qualitative agreement in the expected value sense, while traditional  
221 pulse pair velocities are aliased. The pulse-pair velocities shown herein correspond to a pulse  
222 repetition time of 247 micro-seconds. However, the conventional pulse-pair measurements have  
223 a lower standard deviation than the FDPP estimates of Doppler velocity. This is because of  
224 some inevitable loss of coherence due to frequency swinging. However, given that pulse-pair  
225 estimates are already available in the time-series, one may use the FDPP as a reference to unfold  
226 traditional pulse-pair estimates. In this manner, the higher Doppler Nyquist interval of the FDPP  
227 may potentially be combined with the lower standard deviation of the pulse-pair estimates. Lastly,  
228 the simulated statistics using the aircraft speed projections as input are in qualitative agreement  
229 with measurements for dwell times of 0.5 seconds. This validates the simulation methodology  
230 and the deductions made herein.

231 Fig. 5 shows Doppler velocity estimates made with the traditional pulse-pair algorithm and the  
232 frequency diverse method investigated herein. Here, the surface is at an altitude that is nearly  
233 0 km while a thin layer of cirrus cloud is at an altitude of approximately 7.5 km. We see  
234 that there is little folding in the FDPP and traditional pulse-pair measurements from surface  
235 echoes with little motion along the radial direction. But the additional motion of the cirrus cloud  
236 makes traditional pulse-pair estimates of Doppler velocity fold, as evident from the abrupt color  
237 changes in the image. We also note that the FDPP algorithm yields noisier estimates on clouds  
238 as compared to a nearly static surface. This can be attributed to the loss in coherence in clouds

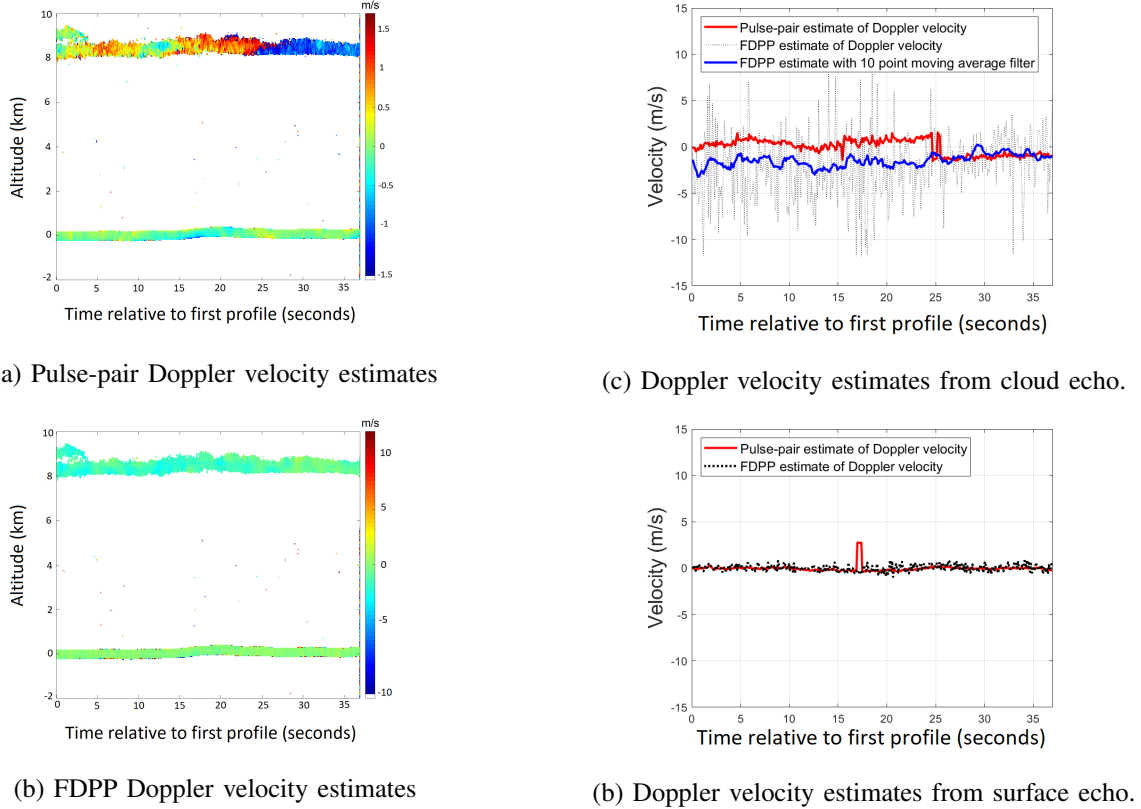


Fig. 5: Cloud radar System (CRS) Doppler velocity measurements from the NOAA GOES-R validation campaign. The dataset was collected on May 17th, 2017 at 03:53 UTC with the antenna was pointing “nearly” at nadir. (a) - Traditional pulse-pair measurements in clouds show significant folding over the flight segment. (b) - Frequency Diverse Pulse-pair measurements (FDPP) in clouds show little folding over the same flight segment. The different color scales used in (a) and (b) reflects the wider Doppler velocity Nyquist interval of the FDPP. But a significant difference in FDPP performance on cloud and surface echoes is shown in subsequent plots. (c) Pulse-pair and FDPP Doppler velocity estimates from a range bin in the cloud layer. Due to low coherence, the FDPP Doppler velocity estimate in the cloud layer has significant random error. But with additional averaging, it can serve as a reference to unfold systematic errors in the cloud-layer pulse-pair estimates. (d) Pulse-pair and FDPP Doppler velocity estimates from surface echoes. Unlike the cloud echo case, the FDPP estimate from surface echoes has significantly better precision and obviates the need for additional averaging. Some folding in the pulse-pair estimates is visible at a relative time of approximately 17 seconds.

relative to surface echoes. For the dataset shown here, the mean coherence in the surface echoes was 0.92 corresponding to the time-lag 33 micro-seconds. This high coherence is qualitatively consistent with the demonstration of orthogonal frequency division multiplexed waveforms for synthetic aperture radar imaging of nearly static surfaces in [20] and [21]. However, the mean coherence in the cloud layer was 0.06. The reason we get some coherent Doppler velocity structure in the clouds is because significant phase anti-correlation results in a cancellation of the variances of the  $f_1/f_2$  and the  $f_2/f_1$  pairs. Contrarily, we see that there is significantly less folding in the FDPP Doppler estimate in the cloud layer compared to traditional pulse-pair Doppler measurements. This shows that the frequency diversity algorithm investigated herein has a wider Nyquist interval for the Doppler velocity estimate relative to traditional pulse-pair measurements. However, it appears based on data that the FDPP Doppler estimates from surface echoes have significantly better precision than Doppler retrievals in clouds. Further research is necessary in order to quantitatively characterize the performance of the FDPP algorithm as a function of surface and volumetric scattering.

#### IV. SUMMARY

Waveforms with frequency diversity have been employed for mitigating the range-Doppler ambiguity dilemma in automotive radars [11]. The novel part of this work was the error canceling algorithm design and the demonstration in a beam-filled scenario. With modern waveform generation, digital receiver and solid-state power amplifier technologies, the frequency diversity algorithm can be implemented without additional hardware such as a second millimeter wave receiver chain. The transmit waveform sequence was multiplexed in time through the transmitter and already available electronics in the radar system. On receive, digital filters isolate returns from each of the frequencies. During the first PRT, the radar system transmitted a sequence of two pulses modulated by frequencies  $f_1$  and  $f_2$  in that order. During the next PRT, the order of the pulses is reversed as  $f_2$  and  $f_1$ . The sum of the phase estimates from the  $f_1/f_2$  and  $f_2/f_1$  pairs yields a composite phase which is linearly proportional to Doppler velocity.

The algorithm concept was investigated using Monte-Carlo simulations and data collected with the NASA GSFC's Cloud Radar System. A simple point-target based analytical formulation enabled interpretation of results. Simulations were employed to go between point-target and surface scattering. On data collected with the NASA Cloud Radar System, the surface echo

269 Doppler estimates made with the FDPP algorithm were in reasonable agreement with traditional  
270 pulse-pair velocities for near-nadir scenarios. On a flight where aircraft maneuvers were performed  
271 to result in high antenna pitch angles, the pulse-pair Doppler velocities from the surface were  
272 aliased while the FDPP Doppler estimate was in agreement with projected aircraft speed. The  
273 algorithm was found to perform well for a spectrum width of about 0.5 m/s and SNR greater than  
274 20 dB. There were two mechanisms for error reduction. First, the phases due to the difference  
275 frequency from the  $f_1/f_2$  and  $f_2/f_1$  pairs canceled out in the expected value sense. Second, the  
276 sum of the two phase estimates has a much smaller variance relative to the individual phase  
277 estimates since the  $f_1/f_2$  and  $f_2/f_1$  phase estimates are highly anti-correlated.

278 FDPP Doppler estimates in clouds were found to have lower precision than surface echoes.  
279 However, the lack of sufficient SNR in clouds made it difficult to attribute differences in precision  
280 due to the volumetric scattering mechanism alone. Future work may focus on adapting the FDPP  
281 algorithm for probing solid planetary surfaces [22] in the context of landing radars. It may  
282 also be worthwhile to investigate other orthogonal waveform designs [20] for Doppler velocity  
283 estimation.

#### 284 ACKNOWLEDGMENT

285 This research was initially carried out at the NASA/Goddard Space Flight Center under  
286 the NASA Instrument Incubator Program award NNH13ZDA001N. Further research and paper  
287 development continued at the Jet Propulsion Laboratory (JPL), California Institute of Technology,  
288 under a contract with the National Aeronautics and Space Administration. At the time of  
289 completing the work, Vijay Venkatesh and Hayk Hovhannisan were supported by the JPL  
290 Research and Technology Development Award 01SCTR/R.18.021.070. Gerard Masalias Huguet  
291 significantly assisted in the preparation of the manuscript. The authors thank Dragana Perkovic-  
292 Martin and Daniel Esteban Fernandez for critiques and numerous discussions that shaped the  
293 manuscript. © 2019. All rights reserved.

#### 294 REFERENCES

- 295 [1] R. Tanamachi, H. Bluestein, W. Lee, M. Bell, and A. Pazmany, "Ground-based velocity track display (gbvtd) analysis of  
296 w-band doppler radar data in a tornado near stockton, kansas on 15th may 1999," *Mon. Wea. Rev.*, pp. 783–800, 2007.  
297 [2] L.Li, G. Heymsfield, P. Racette, L. Tian, and E. Zenker, "A 94 ghz cloud radar system on a nasa high-altitude er-2 aircraft,"  
298 *J. Atmos. Oceanic. Tech.*, vol. 21, pp. 1378–1388, 2004.

- 299 [3] G. Stephens, "The cloudsat mission and the a-train : A new dimension of space-based observations of clouds and  
300 precipitation," *Bull. Amer. Meteor. Soc.*, vol. 83, pp. 1771–1790, 2002.
- 301 [4] J. Stambaugh and R. Lee, "The 4 ghz bandwidth millimeter wave radar," pp. 64–76, 2012.
- 302 [5] S. Patole, M. Torlak, D. Wang, and M. Ali, "Automotive radars : A review of signal processing techniques," *IEEE Sig.  
303 Proc. Mag.*, vol. 34, pp. 22–35, 2017.
- 304 [6] G. Brookner, D. Birch, and J. Solms, "W-band airborne interrupted frequency modulated cw imaging radar," *IEEE Trans.  
305 Aerosp. Electron. Syst.*, vol. 41, pp. 995–972, 2005.
- 306 [7] F. Sajadi, M. Helgeson, M. Radke, and G. Steyn, "Radar synthetic vision system for adverse weather aircraft landing,"  
307 *IEEE Trans. Aerosp. Electron. Syst.*, vol. 35, pp. 2–14, 1999.
- 308 [8] M. Sachidananda and D. Zrnic, "Unambiguous range extension by overlay resolution in staggered prt technique," *IEEE  
309 Trans. Geosci. Electron.*, vol. 17, pp. 113–128, 1979.
- 310 [9] A. Pazmany, J. C. Galloway, J. Mead, I. Popstefanija, R. McIntosh, and H. Bluestein, "Polarization diversity pulse-pair  
311 technique for millimeter wave doppler radar measurements of severe storm measurements," *J. Atmos. Oceanic. Tech.*,  
312 vol. 16, pp. 1900–1911, 1999.
- 313 [10] A. Battaglia and S. Tanelli, "Polarization diversity for millimeter wave spaceborne doppler radars: An answer for observing  
314 deep convection ?" *J. Atmos. Oceanic. Tech.*, vol. 30, pp. 2768–2787, 2013.
- 315 [11] M. Kronauge and H. Rohling, "New chirp sequence radar waveform," *IEEE Trans. Aerosp. Electron. Syst.*, vol. 50, pp.  
316 2870–2877, 2014.
- 317 [12] G. Heymsfield and L. Miller, "Method for ambiguity resolution in range-doppler measurements," *US patent*, Issued Jan.  
318 4, 1994.
- 319 [13] H. Rohling and M. M. Meinecke, "Waveform design principles for automotive radar systems," *Proceedings of the CIE  
320 International conference on radar*, Beijing, 2001.
- 321 [14] R. J. Doviak, R. J. Lataitis, and C. L. Holloway, "Cross correlations and cross spectra for spaced antenna wind profilers  
322 part i: Theoretical analysis," *Radio Sci.*, vol. 31, pp. 157–180, 1996.
- 323 [15] M. Sachidananda and D. Zrnic, "Recovery of spectral moments from overlaid echoes in a doppler weather radar," *IEEE  
324 Trans. Geoscience Remote Sensing*, vol. 24, pp. 751–764, 1986.
- 325 [16] D. Zrnic, "Spectral moment estimates from contigous pulse-pairs," *IEEE Trans. Aerosp. Electron. Syst.*, vol. 13, pp. 344–  
326 354, 1977.
- 327 [17] R. J. Doviak and D. S. Zrnić, *Doppler Radar and Weather Observations*, 2nd ed. Academic Press, 1993.
- 328 [18] V. Venkatesh and S. J. Frasier, "Simulation of spaced antenna wind retrieval performance on an x-band active phased-array  
329 weather radar," *J. Atmos. Oceanic. Tech.*, vol. 30, pp. 1447–1459, 2013.
- 330 [19] W. Lee, P. Dodge, F. Marks, and P. Hildebrand, "Mapping of airborne doppler radar data," *J. Atmos. Oceanic. Tech.*,  
331 vol. 11, pp. 572–578, 1994.
- 332 [20] G. Krieger, "Mimo-sar : Opportunities and pitfalls," *IEEE Trans. Geoscience Remote Sensing*, vol. 52.5, pp. 2628–2645,  
333 2014.
- 334 [21] D. Giuli, M. Fossi, and L. Facheris, "Radar target scattering matrix measurement through orthogonal signals," *IEEE  
335 Proceedings*, vol. 140.4, pp. 233–242, 1993.
- 336 [22] J. Eichler, "A performance study of the lunar module's landing radar system," *Journal of Spacecraft and Rockets*, pp.  
337 1016–1022, 1968.